

# **PREDICTION MODEL FOR OXIDE THICKNESS ON ALUMINUM ALLOY CLADDING DURING IRRADIATION**

Yeon Soo Kim, G.L. Hofman, N.A. Hanan and J.L. Snelgrove

Nuclear Engineering Division

Argonne National Laboratory, 9700 South Cass Avenue, Argonne, IL 60439 – USA

## **ABSTRACT**

An empirical model predicting the oxide film thickness on aluminum alloy cladding during irradiation has been developed as a function of irradiation time, temperature, heat flux, pH, and coolant flow rate. The existing models in the literature are neither consistent among themselves nor fit the measured data very well. They also lack versatility for various reactor situations such as a pH other than 5, high coolant flow rates, and fuel life longer than ~1200 hrs. Particularly, they were not intended for use in irradiation situations. The newly developed model is applicable to these in-reactor situations as well as ex-reactor tests, and has a more accurate prediction capability. The new model demonstrated with consistent predictions to the measured data of UMUS and SIMONE fuel tests performed in the HFR, Petten, tests results from the ORR, and IRIS tests from the OSIRIS and to the data from the out-of-pile tests available in the literature as well.

## **1. Introduction**

The existing models [1–5] to predict oxide thickness on aluminum alloy are neither consistent among themselves nor fit the measured data very well. In addition, the application ranges of all the models are limited, which do not fit various reactor situations such as a pH other than 5, high coolant flow rates, and fuel life longer than ~1200 hrs. Therefore, a new model is needed which is applicable to these in-reactor situations.

An empirical model consisting of correlations predicting the oxide film thickness on aluminum alloy cladding was developed as a function of irradiation time, cladding surface temperature, heat flux at cladding surface, coolant pH, and coolant flow rate at the relevant coolant channel. The model was validated by comparing model predictions to the measured data from in-reactor tests and out-of-reactor data.

## **2. Existing Models**

There were three models available in the literature for oxide thickness predictions. All of them are power law models and were developed for data from out-of-pile loop tests. Because of the limitations in their original data, these models have limited ranges of applicability; for example, all of them were intended to be used for one pH, which is pH of 5, and restricted flow rate.

In addition, irradiation effect was not considered in these models. In order to be used for various in-reactor situations, therefore, the models needed to be stretched to outside of the intended applicability.

The rate equation for oxide growth on aluminum metal or alloy can be expressed by

$$\frac{dx}{dt} = k x^{-p} \quad (1)$$

where  $x$  is the film thickness,  $t$  time,  $k$  is a rate constant, and  $p$  the rate law power. The existing models used this rate equation. The integration of Eq.(1) gives the general form of the kinetic equation of aluminum alloy corrosion:

$$x = \left[ x_0^{p+1} + (p+1) k t \right]^{\frac{1}{p+1}} \quad (2)$$

where  $x_0$  is the film thickness at time zero.

The Griess model was developed in 1960s [1,2]. It used the kinetic equation given in Eq.(2) with  $p=0.28535$ , after fitting  $p$  with their loop test data:

$$x = \left( x_0^{1.28535} + 1.28535 k t \right)^{0.778} \quad (3)$$

where

$x$  = film thickness in  $\mu\text{m}$  at time  $t$   
 $x_0$  = film thickness in  $\mu\text{m}$  at time zero  
 $t$  = time in hr.

The rate constant  $k$  was expressed by

$$k = 1.2538 \times 10^5 \exp\left(\frac{-5913}{T_{x/c}}\right) \quad (4)$$

where  $T_{x/c}$  = temperature at the oxide-water interface (or cladding surface temperature) in K. In this paper, the temperature at the oxide-water interface and the cladding surface temperature are the same so they are used interchangeably.

As seen in Eq.(4), the rate constant is only dependent on the temperature at the oxide-water interface. The other variables, which affect the growth rate, were assumed fixed. Therefore, the Griess model is only applicable for cases that have pH 5, water flow rate of  $\sim 12$  m/s and short duration of 10 – 20 days.

The Kritz model [3] has the same kinetic equation as the Griess model, i.e., Eq.(3). The rate constant, however, was varied by multiplying with heat flux to the power of 1.28535 as well as using different pre-exponential constant and activation energy:

$$k = 8.686 q^{1.28535} \exp\left(\frac{-2416.5}{T_{x/c}}\right) \quad (5)$$

where  $q$  is heat flux at the oxide-water interface in  $\text{MW/m}^2$ . The application range of the Kritz model is similar to that of the Griess model.

An updated version of ANS Correlation II was reported by Pawel, et al. [4–6]. They adopted the same kinetic equation given in Eq.(2) with  $p=0.351$ :

$$x = \left(x_0^{1.351} + 1.351 k t\right)^{0.74} \quad (6)$$

The corresponding rate constant was

$$k = 6.388 \times 10^7 \exp\left(\frac{-9154}{T_{x/c} + 1.056 q}\right) \quad (7)$$

Notice that the reaction temperature is increased by heat flux. The Pawel model also has an application range similar to the other models.

### 3. Proposed New Model

Aluminum alloys undergo oxidation if oxygen is available even at room temperature, producing a protective oxide ( $\text{Al}_2\text{O}_3$ ). The growth rate levels off in a short period. The rate law for this type of oxidation ranges from parabolic to cubic: the rate law power in Eq.(1) for this case is  $p=1$  to 2. The protective oxide, however, degrades in water by hydration forming various oxide-hydrates at the outer surface in time, leaving only a thin protective  $\text{Al}_2\text{O}_3$  layer on the aluminum surface. The most frequently found oxide-hydrates in typical tests are boehmite ( $\text{Al}_2\text{O}_3 \cdot \text{H}_2\text{O}$ ) and bayerite ( $\text{Al}_2\text{O}_3 \cdot 3\text{H}_2\text{O}$ ). Typically, the bayerite layer is found at the outer surface of the boehmite layer. These oxide hydrates are soluble in water, especially in flowing water, meaning that even the hydrated oxide becomes less protective to further enhance film growth. As tests of prefilm samples showed [7], because boehmite has a higher solubility than bayerite, dissolution is selective. In other words, dissolution may take place not exclusively at the oxide-water interface, but within the oxide if cracks and fissures are available. This leaching action increases the porosity of the oxide film. Dillon found that oxide films tested with higher flow rates tend to have higher porosity than with lower flow rates [8].

For oxidation with degraded films, the growth law ranges between linear and parabolic (i.e.,  $0 \leq p \leq 1$ ), depending on the extent of oxide degradation. The degradation of  $\text{Al}_2\text{O}_3$  and oxide-hydrates is dependent on temperature, water pH, water flow rate, and perhaps irradiation.

The deficiency in the existing models primarily lies in their inability to cope with various situations where a different rate law is required according to the extent of oxide degradation. They all use the same rate law regardless of the property of the oxide film.

In this work, the term “film thickness” generally refers the total thickness of the layers of the protective oxide ( $\text{Al}_2\text{O}_3$ ) and hydrated oxide ( $\text{Al}_2\text{O}_3 \cdot \text{H}_2\text{O}$  and  $\text{Al}_2\text{O}_3 \cdot 3\text{H}_2\text{O}$ ).

Dillon [8] showed that the oxide growth increase with increased oxide solubility. Dickinson and Lobsinger [9] reported the solubilities of oxide and oxide-hydrates as a function of temperature and water pH. The higher the temperature and pH, the higher the solubility. They also showed that the oxide dissolution rate increases as the water flow rate increases by increasing the porosity in the oxide films as well as by effectively removing the buildup of dissolved oxide concentration in water.

For the present modeling, the solubility of oxide was formulated based on the equation and data reported in Refs. 8 and 9 as follows:

$$\ln C_s = -\left(\frac{1211.16}{T_{x/c}} + 13.79\right)(1.81 - 0.14 H) \quad (8)$$

where  $C_s$  is the oxide solubility in g/g  $\text{H}_2\text{O}$ ,  $T_{x/c}$  the oxide-water interface temperature in K and  $H$  pH. Here the valid temperature range used is  $25 - 300^\circ\text{C}$  and the pH range is  $5.1 - 7$ . The solubilities at the pH range of  $4.9 - 5.1$  were approximately constant with the same value at pH=5.1. Note that Eq.(8) assumes an infinite dilution at the oxide surface. The flow rates in typical reactors are high enough so that this requirement is satisfied. There was no data for oxide dissolution as a function of flow rate. The data reported by Griess [2] and Pawel [5,6] were used to fit the rate law power  $p$  as a function of  $C_s$  and an augmentation constant  $B$  versus flow rate, simultaneously. As a result, we obtained

$$p = 0.119 + 9.223 \exp(-1.467 \times 10^8 C_s) \quad (9)$$

and

$$B = 0.4264 + \frac{3.2134}{1 + \exp\left(-\frac{v_c - 13.3905}{3.5994}\right)} \quad (10)$$

where  $C_s$  is the oxide solubility given in Eq.(8) and  $v_c$  the coolant flow rate in m/s. The range of coolant velocity fitted is  $3 - 28$  m/s. In Figs. 1 and 2 the curve fitting results are compared with the data.

As a result, the new prediction model can be expressed as follows:

$$x = A B \left[ \left( \frac{x_0}{A B} \right)^{p+1} + (p+1) k t \right]^{\frac{1}{p+1}} \quad (11)$$

Here  $A$  is an augmentation constant depending on the specific reactor conditions. We found that,  $A$  was taken to be unity for out-of-pile data, whereas the best fit for in-reactor data such as HFR tests was obtained with  $A=2$ . This suggests that the in-reactor situation, mainly the irradiation effect, is more favorable for oxide growth.  $B$  and  $p$  are given in Eqs.(9) and (10), respectively. The rate constant  $k$  was derived as described below.

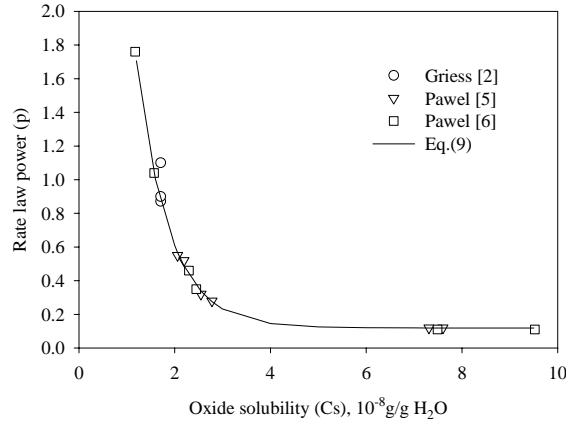


Fig.1 Curve fitting of rate law power ( $p$ ) as a function of Oxide solubility ( $C_s$ ).

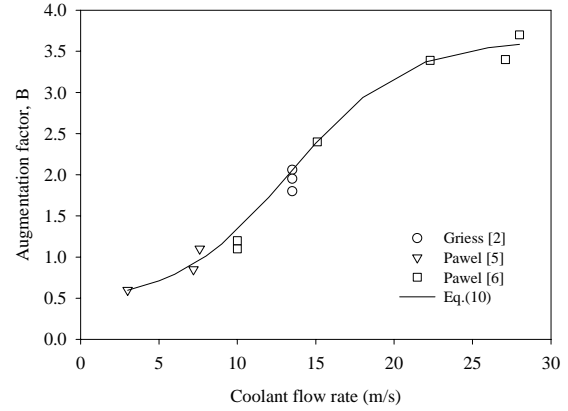


Fig.2 Curve fitting of augmentation factor ( $B$ ) as a function of flow rate ( $v_c$ ).

The temperature drop across the oxide film can be calculated by

$$\Delta T = \frac{q x}{k_T} \quad (12)$$

where  $\Delta T$  is in K,  $q$  is the heat flux in  $MW/m^2$ ,  $x$  the oxide film thickness in  $\mu m$ , and  $k_T$  the effective thermal conductivity of the oxide film in  $W/m-K$ .

The oxide film develops cracks under a high heat flux due to stress buildup, which is another mechanism for porosity increase in the oxide film together with heterogeneous oxide dissolution. The stress buildup is proportional to the temperature drop across the oxide film. The cracking is the direct cause for oxide spallation encountered frequently in thick oxide films. Neither Pawel nor Kritz tried to predict the time of spallation; however, they noticed that the higher heat flux reduces the apparent activation energy, yielding a higher growth rate. Although the heat flux effect is manifested by a combination of other variables such as the oxide thickness and its thermal conductivity, they added a constant increase proportional to the heat flux, and neglected the oxide thickness change and assumed a constant thermal conductivity of the oxide film, e.g.,  $2.25 W/m-K$  [2,5]. For these reasons, their models cannot predict the accelerated film growth as the oxide thickens, particularly near spallation. In the new model, the effect of the porosity buildup due to cracking and heterogeneous oxide dissolution on the oxide film growth was modeled considering the following. The oxide thermal conductivity decreases as the oxide thickens, and the reaction temperature varies as a function of oxide thickness, thermal conductivity, and heat flux.

Postirradiation micrographs [1,5,11,13] revealed that thin oxide films were free of cracks or pores, which suggested that the thermal conductivity degradation of thin oxides was negligible. As the oxide film thickened further, however, its thermal conductivity decreased due to porosity increase. After reviewing the data [1-5,10-13], the threshold thickness was tentatively set at 25  $\mu\text{m}$ . The decrease was assessed by an empirical function of the oxide thickness at a rate giving  $k_T = 1.85 \text{ W/m-K}$  at  $x = 50 \mu\text{m}$ . This rate was deduced from the data reported by Griess [1]. The temperature dependence of the oxide thermal conductivity was not available in the literature. Therefore, it was considered constant with respect to temperature. Consequently, the oxide thermal conductivity as a function of the oxide film thickness was formulated by

$$\begin{aligned} k_T &= 2.25, & \text{for } x \leq 25, \\ k_T &= 2.25 - 0.016(x - 25), & \text{for } 25 \leq x \end{aligned} \quad (13)$$

where  $k_T$  is in W/m-K and  $x$  in  $\mu\text{m}$ .

The reaction temperature of Griess and Kritz models is the temperature at the oxide-water interface although they use the rate constants fitted to the oxide thickness data. As seen in Eq.(7), the reaction temperature of the Pawel model was obtained by adding a term linearly proportional to the heat flux to the oxide-water interface temperature. Therefore, all the existing models basically use a fixed reaction temperature regardless of the oxide thickness and property.

The reaction temperature governing the Al oxidation reaction in steam is known as the metal-oxide interface temperature [1,10]. This suggests that the oxidant transport in the oxide governs the overall reaction process. In water, however, although the oxidant transport in the oxide becomes important, the temperature deciding the overall reaction would be located somewhere between the metal-oxide and oxide-water interfaces, considering the easier access of water through the defected oxide. For low values of the temperature difference  $\Delta T$  across the oxide film, the use of oxide-water interface temperature is considered acceptable. However, for situations with high  $\Delta T$  values, which prevail under situations of a thick film with high porosity and a high heat flux, this causes considerable underpredictions. In addition,  $T_{x/c}$  is fixed in time once the coolant temperature is set. Therefore, the rate constant  $k$  of the existing models is constant throughout the calculation. In reality,  $k$  must vary as the oxide film thickens and porosity in the oxide film changes. After fitting the data [5,6,11,13],  $k$  was correlated as follows:

$$k = 1.95 \times 10^5 \exp \left( \frac{-6071}{T_{x/c} + a \frac{q x}{k_T}} \right) \quad (14)$$

where  $a$  is a constant;  $a=0.05$  for out-of-pile data [2,5,6] and  $a=0.37$  for in-reactor data [11,13]. Notice that  $T_{x/c}$  and  $q$  are fixed by the reactor operation scheme, and  $x$  and  $k_T$  are changing as irradiation enhances. The time interval optimized in fitting  $a$  was 24 hours and, for  $x$ , the value at the previous time step was used to avoid endless iteration.

The effect of CRUD, found in an outer Fe-rich layer on the corrosion films, was taken into account in  $k$  implicitly. The typical CRUD layer from loop tests was 1~2  $\mu\text{m}$  and its buildup reduces the underlying corrosion product growth [5]. The CRUD deposition rate was known to be minimal for most reactor situations where the coolant pH was higher than 5 and inlet temperature was high enough [4].

The Griess data [1,2] were obtained for alloy 6061 and 1100, the Kritz data [3] were for 8001, and the Pawel data [4–6] were for pure Al, 1100, 6061 and 8001. The authors found no significant difference in the oxidation rate of these alloys, although different behavior associated to spallation and internal reactions was observed. Therefore, it is our view that the new model is also applicable equally to these alloys.

Other parameters noticed to affect the oxidation rate were coolant electrical conductivity and coolant inlet temperature. These parameters were not incorporated into the model because they were redundant to the variables already in the correlations.

#### 4. Model Validation

In order to calculate the oxide thickness, the new model needs information on cladding surface temperature, heat flux at the cladding surface, pH, and coolant flow rate at the coolant channel as a function of time. The model constants  $A=1$  and  $a=0.05$  were used for out-of-reactor data given in Figs. 3 and 4, and for any reactor cases  $A=2$  and  $a=0.37$  were used.

Figs.3 and 4 show comparisons between the predictions by the new model and the existing models with the measured data reported by Pawel [5]. The new model predictions are the closest to the data for all the cases and the Griess model follows. It is remarkable that the Pawel model does not predict well their data.

In figures 5 and 6 the measured data from the UMUS tests in HFR, Petten [11] are compared with the predictions by the new model. The measured film thickness data were obtained from the optical metallographic pictures of Ref. 11. Temperatures were calculated based on the power histories of HFR Petten. The axial heat flux distribution was obtained based on the gamma scan result, and the plate powers were available from ANL-CEA joint work [12]. The coolant enters from the top of the core in the UMUS and SIMONE tests [11,13].

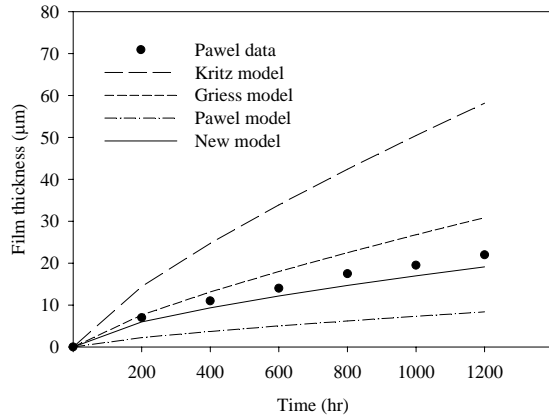


Fig.3 Comparison of model predictions with data from Pawel [5].  
The data were for NPR Test A-2 (position 4) with  
 $T_{x/c}=130^{\circ}\text{C}$ ,  $q=3.8 \text{ MW/m}^2$ ,  $\text{pH}=5.4$  and  $v_c=7.6 \text{ m/s}$ .

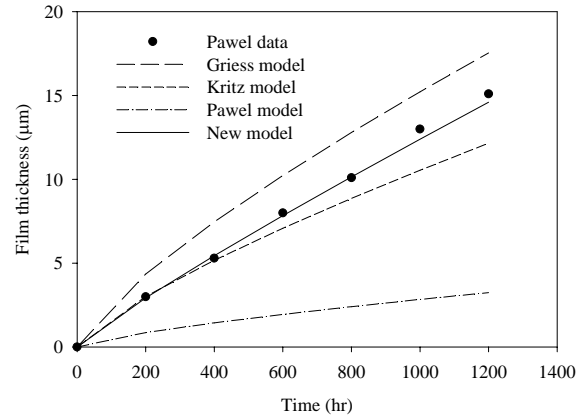


Fig.4 Comparison of model predictions with data from Pawel [5].  
The data were for NPR Test A-4 (position 4) with  
 $T_{x/c}=111^{\circ}\text{C}$ ,  $q=1.0 \text{ MW/m}^2$ ,  $\text{pH}=6.0$  and  $v_c=3.0 \text{ m/s}$ .

The error bar indicates the range of the minimum and maximum of the measured data in the sample. The MEU test, shown in Fig. 6, experienced oxide spallation. This behavior was well simulated by the model: the accelerated film growth in a short period at the final stage of the test indicates the possibility of spallation.

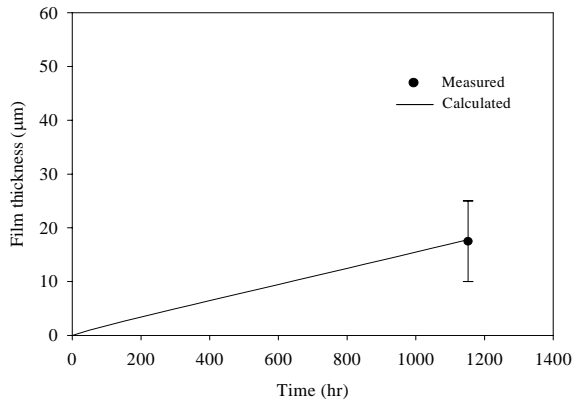


Fig.5 UMUS U7MR2005 (LEU) sample at 90 mm from bottom.  
 $T_{x/c}=82.6^{\circ}\text{C}$ ,  $q=1.7 \text{ MW/m}^2$ ,  $\text{pH}=6.5$  and  $v_c=8.3 \text{ m/s}$ .

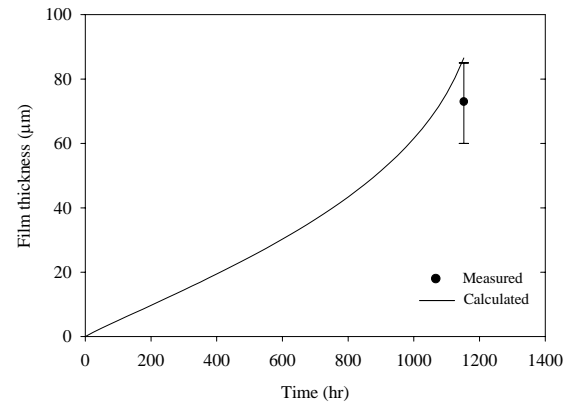


Fig.6 UMUS U7MR3505 (MEU) sample at 274 mm from bottom.  
 $T_{x/c}=107.4^{\circ}\text{C}$ ,  $q=2.5 \text{ MW/m}^2$ ,  $\text{pH}=6.5$  and  $v_c=8.3 \text{ m/s}$ .

Two predictions were made and shown in Figs. 7 and 8 for the SIMONE tests [13]. The measured film thickness data were obtained from the optical metallographic pictures contained in Ref. 13. Cladding surface temperatures and heat flux were calculated based on the power histories, coolant flow condition, and inlet temperatures supplied by the HFR and also included in the figures. For both samples, the predictions were made with the power history of the average power plate. A slight underprediction was observed for the top sample shown in Fig.8. The reason is not known at this time.

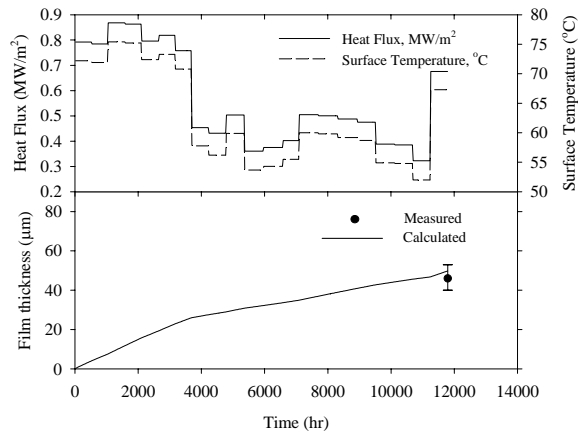


Fig.7 SIMONE LC-04 measured at the center of the test plate  
(Test in HFR: pH=6.5,  $v_c=6.6$  m/s).

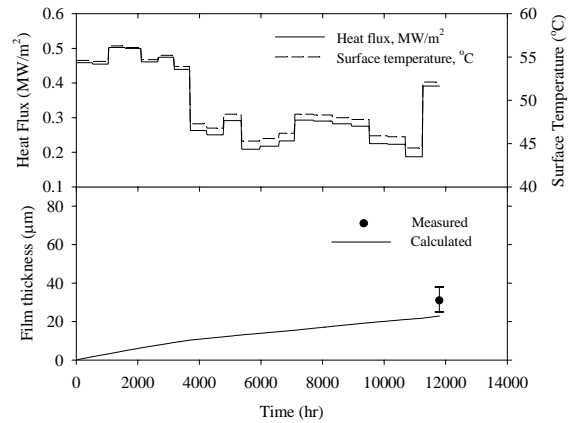


Fig.8 SIMONE LC-04 measured at the top of the test plate where coolant enters (Test in HFR: pH=6.5,  $v_c=6.6$  m/s).

A calculation for the miniplate test from ORR was made, and the results are shown in Fig.9. The miniplate is approximately one-fifth of the standard plate in length and flat plate type, in contrast to the curved plates of the standard case. Five modules including the reduced-length plates were stacked in a module holder. The oxide thickness measurement was made at the center of the plate A101. The heat flux and surface temperature of the A101 plate were calculated based on the power history. The position of the module in the holder, however, was not identified. The center location for the module was assumed.

In Fig.10, the results for a standard plate test are shown. Two calculations were made for the two cases of the power history; the average power throughout the fuel life and the linearly decreasing power from the beginning of life to the end. The prediction by the linearly decreasing power assumption was higher than that by the average power assumption. This implies that the higher power at the beginning of life resulted in a larger oxide thickness.

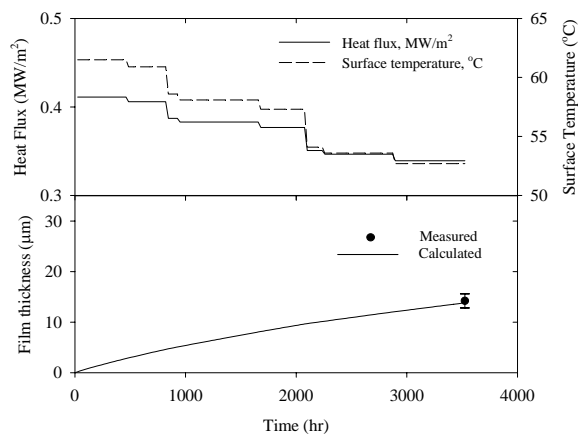


Fig.9 Miniplate A101 (Test in ORR: pH=6.0,  $v_c=8.5$  m/s).

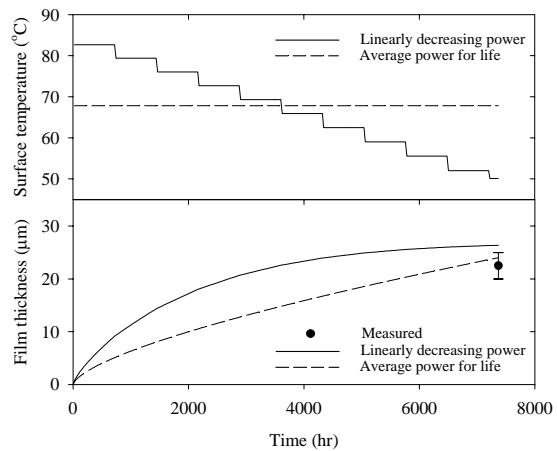


Fig.10 Standard plate BSI-202  
(Test in ORR: pH=5.7,  $v_c=8.1$  m/s).

Fig.11 shows the calculations for IRIS tests in OSIRIS. The power history and cladding surface temperature were retrieved from Ref.14. The IRIS-2 oxide was also calculated although the measured data are not available. For IRIS-1, the prediction was higher than the measured value perhaps because the power and surface temperature used were higher than the real ones. The power and temperature at the plate center were used whereas the oxide measured was at an axial location off the center.

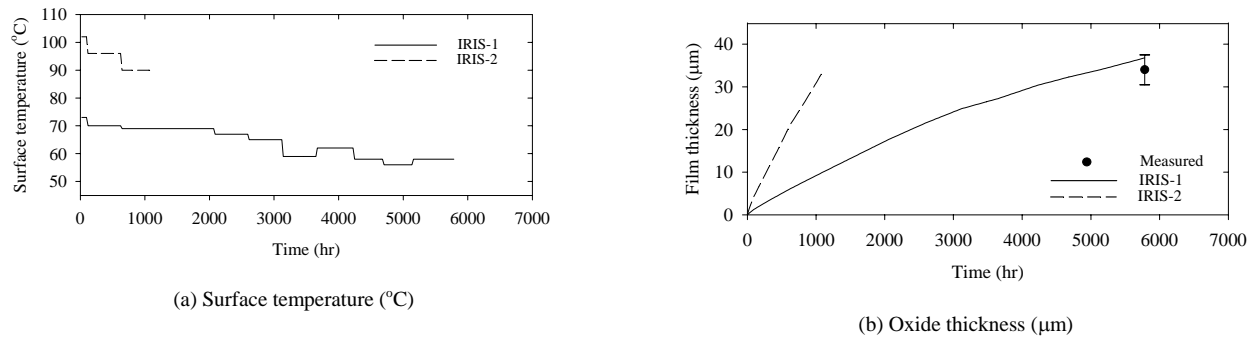


Fig.11 IRIS 1 and 2 tests from OSIRIS (pH=6.0,  $v_c=9.0$  m/s).

In general, the model calculations are close to the measured values, which confirms the validity of the model. However, for some cases, there were inconsistencies of the model predictions to the measured values. These are assumed to result from inaccurate input data, i.e., cladding surface temperature, heat flux, pH and coolant flow rate as a function of time. If an accurate power history is given, the cladding surface temperature and heat flux are calculated accurately. However, coolant flow rate and pH are generally available in a range, which forces average values to be used. This leads to inaccurate results, because the model is sensitive to these input data, particularly in the pH range of 5 – 6.

## 5. Summary

An empirical model for predictions of the oxide film thickness on aluminum alloy cladding was developed as a function of irradiation time, temperature, heat flux, pH, and coolant flow rate. The applicable ranges of the variables cover most reactors. The predictions by the new model were in good agreement with the in-reactor data and out-of-reactor data as well.

For better predictions, precise records of power, pH and coolant flow rate as a function of irradiation time are necessary.

## 6. References

- [1] J.C. Griess, H.C. Savage and J.G. Rainwater, et al., ORNL-3230, Oak Ridge National Laboratory (1961).
- [2] J.C. Griess, H.C. Savage and J.L. English, ORNL-3541, ORNL-3230, Oak Ridge National Laboratory (1964).

- [3] R.S. Ondrejcin, DPST-83-324, Savannah River Laboratory (1983).
- [4] R.E. Pawel, G.L. Yoder, D.K. Felde, B.H. Montgomery and M.T. Mcfee, Oxidation of Metals, 36(1/2), 175 (1991).
- [5] R.E. Pawel, D.K. Felde, J.A. Clinard and T.A. Thornton, Corrosion 93, The NACE annual conference and corrosion show, 188/1 (1993).
- [6] S.J. Pawel, D.K. Felde and R.E. Pawel, Oak Ridge National Laboratory, Report ORNL/TM-13083, October, 1995.
- [7] M.J. Graber, G.W. Gibson, V.A. Walker and W.C. Francis, IDO-16958, US AEC (1964).
- [8] R.L. Dillon, HW-61089, Hanford Laboratory (1959).
- [9] D.R. Dickinson and R.J. Lobsinger, HW-77529, Hanford Laboratory (1963).
- [10] R.L. Sindelar, P.S. Lam, M.R. Louthan, Jr., and N.C. Iyer, Mater. Characterization, 43, 147 (1999).
- [11] A. Languille, G. Hofman, H. Vacelet, et al., ENS RRFM 2002 Transactions, 6<sup>th</sup> International Topical Meeting on Research Reactor Fuel Management, Ghent, Belgium, Mar. 17-20, 2002.
- [12] F. Huet, B. Guidon, P. Lemoine, et al., ENS RRFM 2003 Transactions, 7<sup>th</sup> International Topical Meeting on Research Reactor Fuel Management, Aix-en-Provence, France, Mar. 9-12, 2003.
- [13] G.L. Hofman, Y. Fanjas, H. Pruimboom, and F. Wijtsma, Proc. 16<sup>th</sup> International Meeting on Reduced Enrichment for Research and Test Reactors, Oct. 4 –7, 1993, Oarai, Japan, JAERI report, JAERI-M-94-042, March 1994.
- [14] P. Sacristan, H. Vacelet, J.M. Hamy, et al., ENS RRFM 2003 Transactions, 5<sup>th</sup> International Topical Meeting on Research Reactor Fuel Management, Aachen, Germany, Apr. 1-3, 2003.